

The f.c.c. and h.c.p. lattices differ only in the third and successive neighbours. The coordination numbers (n) up to fifth neighbours are given in Table 1. For a thermodynamic hard-sphere fluid, the pressure at a fixed temperature and volume is directly related to the collision frequency by

$$P^* = \left(1 + \frac{n_c(\tau)\sqrt{\pi}}{3\tau}\right)/V^* \quad (7)$$

wherein n_c is the number of collisions in the time τ . In the stable crystal region only first neighbours collide; one would not expect to find a significant pressure difference in the stable crystal range up to the melting transition because of first-neighbour collision dominance. Likewise, in the lower density region of the SO-cell model, the two respective f.c.c. and h.c.p. structures have identical free energies relative to the ideal gas (RT) and exactly the same low-density equation of state given by the first two terms in equation (5).

Lengthy MD calculation, of the order of 10 million collisions, of the pressure in the SO-cell model in the intermediate density range, however, reveal that there is a region of mechanical instability in which there are significant contributions to pressure from second, third, and, in the h.c.p. case, fourth and fifth neighbour collisions, which differ between f.c.c. and h.c.p. This mechanical instability is a non-physical artefact of the SO-cell nuclei; it appears to be a first-order phase transition from a quasi-crystalline state in which the spheres are localized at the cell centres, to a quasi-fluid state in which the singlet probability density is delocalized within each cell. It is in this region of the mechanical instability transition that this small, but significant, difference in pressure between the two structures is to be found. Extensive MD computations in the SO-cell model, for both f.c.c. and h.c.p. structures, with systems of 500, 2,048 and 12,000 spheres, averaging between 10 million and 100 million collisions for each data point, have been carried out at in the volume range $V^* = 1.00$ – 1.25 .

Figure 1b shows a detailed plot of these pressure data (for the larger systems); it is a $100\times$ expansion of the small dashed square in Fig. 1a. This high-resolution picture of the respective equation-of-state shows clearly that the two structures have quite different properties in the vicinity of the SO-cell model structural instability transition. Moreover, there is a small pressure difference in the immediate region on both sides of the transition of approximately $0.02k_B T/\sigma^3$. On the low-pressure side of the transition, the h.c.p. has the lower pressure, whereas on the high-pressure side of the transition, the f.c.c. has the lower pressure. Interestingly, after numerical integration, these small tail contributions on each side of the transition largely cancel.

Both transitions in the respective SO-cell models show characteristics of a first-order phase transition; an inversion loop for the smaller systems, and transient metastability on either side of the transition. The data in Fig. 1b have been obtained mainly for a system of $N = 2,048$ spheres, with period boundary conditions.

Computations have also been carried out for $N = 500$ and $N = 12,000$ to confirm the interpretation of the present data. The transition pressures for infinite lattices are estimated to be 8.55 and 8.70 for the two structures respectively.

The Gibbs free-energy difference between the two phases is obtained by integrating the area between the f.c.c. and h.c.p. single occupancy isotherms. The result is $G_{\text{hcp}} - G_{\text{fcc}} = 0.005RT$; an equivalent shaded square area is shown in Fig. 1b. Frenkel and Ladd⁷ found no free-energy difference within the uncertainty of their computations ($0.0015RT$, which is less than the difference of $0.005RT$ obtained here). Both their method and mine devise a reversible path connecting the two structures to an idealized state, where the free energy is analytic and the same for both structures. Frenkel and Ladd, however, integrate the free-energy difference over the whole path, because their method cannot identify the physical origin of any such difference. In the single-occupancy model, on the other hand, the source of the difference is a very small region of the whole path, and by focusing the calculation on this region I have been able to quantify this difference.

These computations are being continued to improve the accuracy. From the present SO-cell equation-of-state data, however, it seems clear that the difference in thermodynamic properties between these two crystal structures is significant, amounting to $0.005R$ with an estimated uncertainty of $\sim 20\%$ for the molar entropy. The f.c.c. crystal structure of atomic hard spheres is more stable than the h.c.p. structure by a significant molar Gibbs free-energy difference of $\sim 0.005RT$. Further computations are underway to reduce the small uncertainties arising from the numerical integrations, to assess the effect of imposing isotropy on the h.c.p. structure which has only two-fold symmetry compared to the six-fold f.c.c., and further, to calculate the free energies of alternative hybrid structures of the stacking type-ABCAB—and so on which have not previously been considered at all. None of these considerations, however, are likely to alter the present conclusion that the stable structure of crystalline spheres is face-centred cubic. □

Received 22 July; accepted 11 November 1996.

1. Kittel, C. *Introduction to Solid State Physics* 5th Edn, Ch. 1 (Wiley, New York, 1976).
2. Alder, B. J., Hoover, W. G. & Young, D. A. *J. Chem. Phys.* **49**, 3688–3696 (1968).
3. Stillinger, F. H. & Salsburg, Z. W. *J. Chem. Phys.* **46**, 3962–3975 (1967).
4. Rudd, W. G., Salzberg, Z. W., Yu, A. P. & Stillinger, F. H. *J. Chem. Phys.* **49**, 4857–4863 (1968).
5. Alder, B. J., Carter, B. P. & Young, D. A. *Phys. Rev.* **183**, 831–833 (1969).
6. Alder, B. J., Young, D. A., Mansigh, M. R. & Salzberg, Z. W. *J. Comput. Phys.* **7**, 361–366 (1971).
7. Frenkel, D. & Ladd, A. J. C. *J. Chem. Phys.* **81**, 3188–3193 (1984).
8. Kirkwood, J. G. *J. Chem. Phys.* **18**, 380–382 (1950).
9. Hoover, W. G. & Ree, F. H. *J. Chem. Phys.* **49**, 3609–3619 (1968).
10. Carnahan, N. F. & Starling, K. E. *J. Chem. Phys.* **51**, 635–638 (1979).
11. Woodcock, L. V. *Ann. NY Acad. Sci.* **371**, 274–298 (1981).

CORRESPONDENCE should be addressed to L.V.W. (e-mail: l.v.woodcock@bradford.ac.uk).

TABLE 1 Properties of the first five coordination shells

		Neighbour				
		1st	2nd	3rd	4th	5th
f.c.c.	Number of neighbours	12	6	24	12	24
	Separation/ d_0	1	$2^{1/2}$	$3^{1/2}$	$4^{1/2}$	$5^{1/2}$
h.c.p.	Number of neighbours	12	6	2	18	12
	Separation/ d_0	1	$2^{1/2}$	$(8/3)^{1/2}$	$3^{1/2}$	$(11/3)^{1/2}$

Coordination numbers of the first five coordination shells in the face-centred cubic (f.c.c.) and hexagonal close-packed (h.c.p.) lattice structures. In the single-occupancy (SO)-cell model, at intermediate densities around the vicinity of the phase transition, collisions can occur between third neighbours in the f.c.c. structure, and up to fifth neighbours in the h.c.p. structure.

Single-molecule spectral fluctuations at room temperature

H. Peter Lu & X. Sunney Xie

Pacific Northwest National Laboratory, Environmental Molecular Sciences Laboratory, PO Box 999, Richland, Washington 99352, USA

RECENT advances in near-field¹ and far-field^{2,3} fluorescence microscopy have made it possible to image single molecules and measure their emission^{3,4} and excitation⁵ spectra and fluorescence lifetimes^{3,6–8} at room temperature. These studies have revealed spectral shifts⁴ and intensity fluctuations^{6,7}, the origins of which are not clear. Here we show that spontaneous fluctuations in the spectra of immobilized single dye molecules occur on

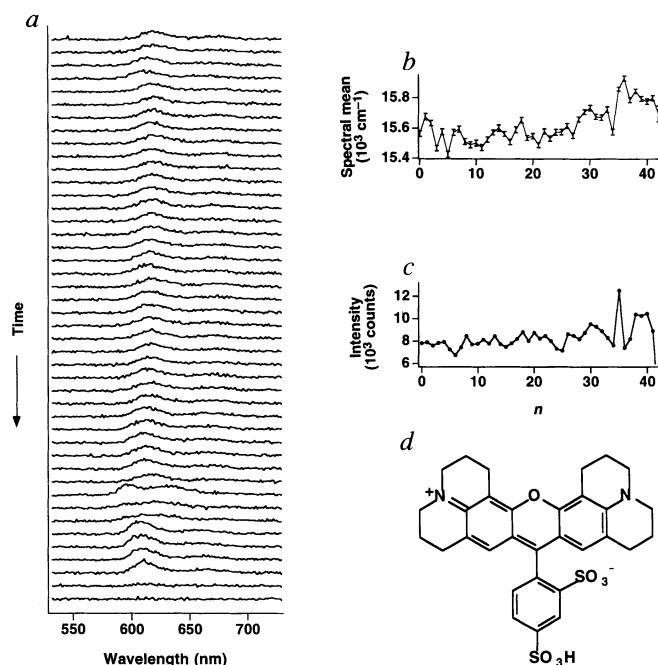


FIG. 1 a, Emission spectra of a single sulphorhodamine 101 molecule taken sequentially with 170-ms data collection times before the final photobleaching. Significant spectral shifts are evident. b, Trajectory of the spectral mean (in wavenumbers) of the molecule; n is the index number of the spectra. The fluctuations are clearly beyond the error bars. c, Trajectory of the total emission intensity (integrated area of each spectrum) of the molecule. d, Structure of the molecule. The emission spectra of individual molecules were recorded with a high emission collection efficiency (10%) using a combination of a spectrograph (Acton Research, Acton) and a back-illuminated CCD camera (Princeton Instruments, Trenton) configured for a spectral resolution of 1 nm with no dead time in data collection.

two different timescales: hundreds of milliseconds and tens of seconds, indicating that these fluctuations have two distinct activation energies. In addition, we see photoinduced spectral fluctuations on repeated photoexcitation of single molecules. We suggest that all of these fluctuations can be understood as transitions between metastable minima in the molecular potential-energy surface.

We obtained diffraction-limited fluorescence images of individual sulphorhodamine 101 molecules with a modified inverted fluorescence microscope (Nikon), in a similar fashion to a recent report³. The sample was prepared by first spin-coating a quartz surface with a 10^{-9} M dye solution and then with a 20-nm polymethylmethacrylate film to prevent fast photobleaching. Figure 1a shows the emission spectra of a single molecule sequentially recorded with 170-ms collection times. The trajectory of the spectral means is shown in Fig. 1b. The fluctuations of the spectral means are evident, while the spectral widths remain essentially constant. In addition, the total emission intensity (that is, the integrated area of each spectrum) fluctuates with time (Fig. 1c) and is consistent with other observations using near-field microscopy^{6,7}. The intensity fluctuations were previously attributed to spectral shifts.⁶ Indeed, the intensity fluctuations (Fig. 1c) essentially correlate with the spectral fluctuations in Fig. 1b: a blue-shifted emission (and absorption) spectrum results in a larger absorption cross-section at the excitation wavelength (532 nm, at the blue edge of the absorption band). The spectra shown in Fig. 1 were taken

with an excitation rate of $5 \times 10^5 \text{ s}^{-1}$, which is much lower than the saturation rate⁹. At saturation, intensity fluctuation arises from a different origin: trapping into the metastable triplet state^{10,11}.

Every molecule that we examined in a large population exhibited similar spectral fluctuations. To evaluate these statistically, we analysed the autocorrelation function $C(t) = \langle v(0)v(t) \rangle - \langle v \rangle^2$ of spectral trajectories, v being the spectral mean in wavenumbers. Each trajectory contained at least several hundred spectra. Figure 2 shows a typical $C(t)$ of a molecule; the trajectory was recorded with an excitation rate of $2.6 \times 10^5 \text{ s}^{-1}$ at 594 nm. The distribution of spectral means (Fig. 2 inset) reflects the transition frequencies accessed by the single molecule in the particular environment. Molecules in different environments have distributions that are significantly different in centre positions (620–680 nm) and in widths (full-widths at half-maximum, 4–20 nm).

The autocorrelation function has a spike at zero time (Fig. 2), due to uncorrelated measurement noise for spectral means (see Fig. 1b for error bars) and spectral fluctuations faster than the time resolution. $C(t)$ can be fitted by a double exponential decay with the spike at zero time:

$$C(0) = \sigma_0^2 + \sigma_1^2 + \sigma_2^2 \quad \text{for } t = 0 \quad (1a)$$

$$C(t) = \sigma_1^2 \exp(-k_1 t) + \sigma_2^2 \exp(-k_2 t) \quad \text{for } t > 0 \quad (1b)$$

The dashed line in Fig. 2 is a fit with a spike, $\sigma_0^2 = 2,000 \text{ cm}^{-2}$; a fast component, $k_1 = 1.9 \text{ s}^{-1}$ and $\sigma_1^2 = 5,000 \text{ cm}^{-2}$; and a slow component, $k_2 = 0.022 \text{ s}^{-1}$ and $\sigma_2^2 = 10,700 \text{ cm}^{-2}$.

To understand the mechanism of these components of spectral fluctuations, we note that molecules do not exhibit noticeable lateral translation beyond a range of a few nanometres. In addition, no detectable variations in the orientation of the transition dipole were observed in this system⁶. Thus we attribute the spectral fluctuations to changes of nuclear coordinates—either the intramolecular coordinates (such as conformations of a side chain) or the intermolecular coordinates (such as hydrogen bonds and collective nuclear coordinates of the interacting environment). The observation that the autocorrelation function of the single molecule has a fast and a slow component implies the existence of at least two quasi-independent distributions of spectral means, with variances of σ_1^2 and σ_2^2 . These two distributions relate to different variations in nuclear coordinates taking place at different rates (k_1 and k_2).

We evaluate the excitation-rate dependence of k_1 and k_2 for many trajectories of many molecules to determine whether the spectral fluctuations are spontaneous or photoinduced. We observed that the fast component (k_1) is independent of excitation rate and excitation wavelength (Fig. 3a), and that the slow

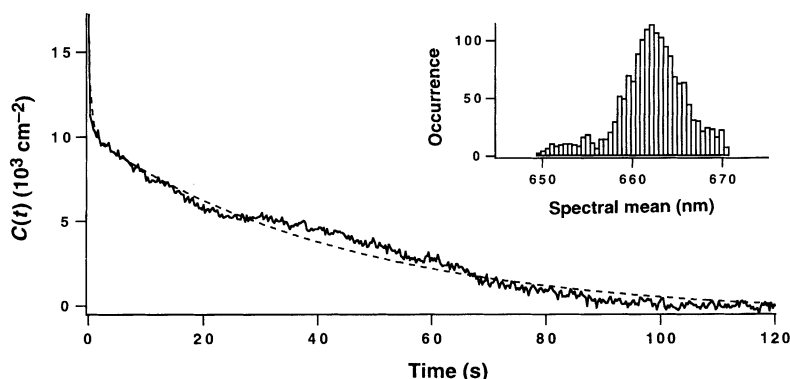


FIG. 2 The autocorrelation function, $C(t) = \langle v(0)v(t) \rangle - \langle v \rangle^2$, derived from the trajectory of spectral means of a single sulphorhodamine 101 molecule at an excitation rate of $2.6 \times 10^5 \text{ s}^{-1}$ at 594 nm. The dashed line is a fit to the data using equation (1b) in the text; parameter values are $k_1 = 1.9 \text{ s}^{-1}$, $k_2 = 0.022 \text{ s}^{-1}$, $\sigma_0^2 = 2,000 \text{ cm}^{-2}$ and $\sigma_2^2 = 10,700 \text{ cm}^{-2}$. Inset, the distribution of the spectral means derived from the same trajectory.

component (k_2) is excitation-rate-dependent and is different for 532-nm (Fig. 3b) and 594-nm excitation wavelengths (Fig. 3c). The excitation rate was varied by adjusting the power of linearly polarized excitation light (0.1–2 μW) and by choosing different molecular orientations. The excitation rates were determined from the integrated area per spectrum by assuming a fluorescence quantum yield close to unity and an emission collection efficiency of 10%. The amplitude ratio of the fast and slow components (σ_1^2/σ_2^2) is essentially independent of the excitation rate, but varies from molecule to molecule.

The observation that the fast component is independent of the excitation rate indicates that the fast fluctuation is spontaneous (known as spectral diffusion) rather than photoinduced. To further confirm this conclusion, we used a shutter to repeatedly block the excitation light for a period of 'dark time', T_{off} , after each spectrum collection time, T_{on} , and obtained the autocorrelation function, $C(n)$ (n being the index number of spectra) (Fig. 4 inset). Figure 4a shows the $C(n)$ of a molecule with $T_{\text{off}} = 0$; Fig. 4b shows the $C(n)$ for the same molecule with a $T_{\text{off}} = 0.5$ s at an identical excitation rate during T_{on} . If no spontaneous fluctuations occurred during the dark times, the two curves of $C(n)$ would be identical. We observe, however, that the fast component of $C(n)$ disappeared in Fig. 4b, which provides additional evidence of the spontaneous fluctuation during the dark times.

At room temperature, spontaneous fluctuations on the sub-picosecond timescale are responsible for the broad spectral widths (Fig. 1a). However, the spontaneous fluctuation we observed on the rather long timescale (hundreds of milliseconds) would be

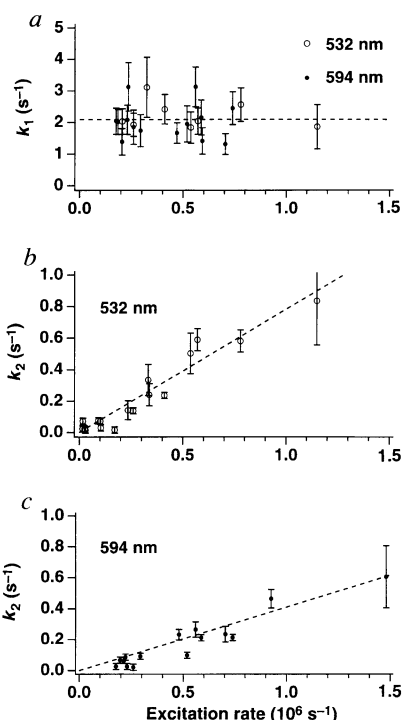


FIG. 3 a, The dependence of k_1 , the fast component of $C(t)$, on the excitation rate. The data points are from different molecules at either 532-nm (open circles) or 594-nm (filled circles) excitation. The independence of k_1 (~ 2.1 s⁻¹) on excitation rate and wavelength indicates that the spectral fluctuation is spontaneous. b, The dependence of k_2 , the slow component of $C(t)$, on the excitation rate with 532-nm excitation. The data points are from different molecules. The quasi-linear relationship indicates that the spectral fluctuation is photoinduced. The quantum efficiency for photoinduced spectral change is 7.8×10^{-7} according to the slope. c, The dependence of k_2 on the excitation rate with 594-nm excitation. A quasi-linear relationship is also observed but with a slower photoinduced fluctuation. The quantum efficiency for photoinduced spectral change is 4.1×10^{-7} . The larger error bars at high excitation rates are associated with the shorter trajectories due to photobleaching.

extremely difficult, if not impossible, to detect at room temperature in ensemble-averaged experiments. Although spontaneous fluctuations^{12,13} have been studied for single molecules at cryogenic temperatures, the room-temperature fluctuations we observed have significantly larger magnitude and involve a thermally activated mechanism (rather than tunnelling).

The quasi-linear dependence of k_2 on excitation rate (Fig. 3b, c) clearly indicates the photoinduced nature of the spectral fluctuations at the longer timescale. Although we cannot rule out the possibility of a quadratic dependence on excitation power, multiphoton processes (such as excited state absorption) are not likely to occur at the low power level ($< 10^3$ W cm⁻²) used.

There are two possible mechanisms for the photoinduced spectral fluctuation. First, a molecule can access other ground-state potential minima with different spectra through relaxations from its singlet excited state, a phenomenon known as 'non-photochemical hole burning'¹⁴. Single-molecule 'nonphotochemical hole burning' has been observed at cryogenic temperature¹⁵⁻¹⁷, but the spectral shifts are much smaller than those observed in our experiment. Second, the spectral fluctuations can also be associated with radiationless relaxations, probably from the triplet state. The energy released in each relaxation event is quickly dissipated into the substrate, and the original temperature of the system is re-established before the next photoexcitation. However, the energy released can lead to variations of the nuclear coordinates, resulting in a new spectrum in subsequent photoexcitations. At present, we are not able to distinguish experimentally between these two mechanisms. The slow rate of photoinduced fluctuation is associated with the small quantum efficiency for either of the two mechanisms. The apparently steeper slope in Fig. 3b is probably associated with the higher photon energy of the 532-nm excitation.

For either the fast or slow spectral fluctuation component, both thermal and photoinduced contributions are possible. Dominated by the thermal fluctuation, k_1 receives little contribution, if any, from the photoinduced fluctuation because of its small quantum efficiency. Conversely, k_2 has some contribution from the thermal

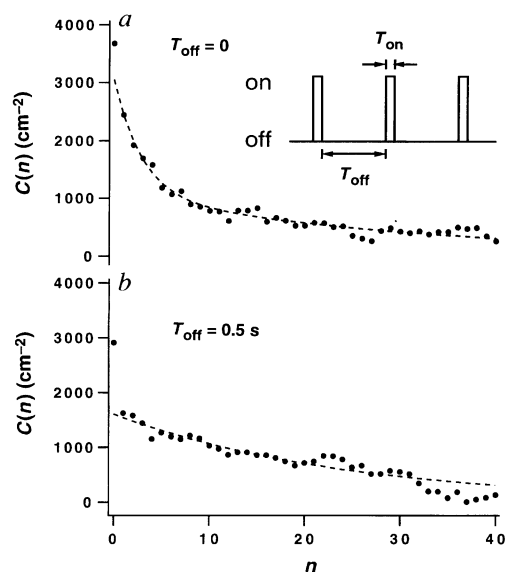


FIG. 4 The inset shows schematically the time dependence of the excitation light; this light is periodically blocked for a dark time, T_{off} , after each spectral collection time, T_{on} (170 ms). a, The autocorrelation function $C(n)$, for a single molecule under continuous 594-nm excitation ($T_{\text{off}} = 0$), n being the index number of the spectra. The dashed line is a double exponential fit, $C(n) = \{2,000 \exp(-0.35n) + 1,050 \exp(-0.03n)\}$ cm⁻². b, The $C(n)$ for the same molecule taken with a dark time $T_{\text{off}} = 0.5$ s and the same excitation rate during T_{on} . The fast component disappears, proving the spontaneous (thermal) fluctuation during the dark time. The dashed line is a single exponential fit with a decay constant $\gamma = 0.04$.

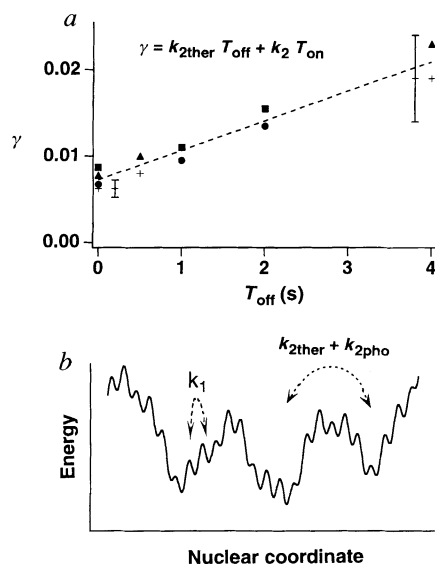


FIG. 5 *a*, Plot of γ , the decay constant of $C(n)$, as a function of the dark time T_{off} . Data points derived from spectral trajectories of the same sulphorhodamine 101 molecule are labelled with the same symbols. The slope of the dashed line gives the slow thermal rate $k_{2\text{ther}} = 0.02 \pm 0.01 \text{ s}^{-1}$, while the intercept gives the photoinduced rate, $k_{2\text{pho}} = 0.02 \pm 0.01 \text{ s}^{-1}$ at the excitation rate of $2 \times 10^5 \text{ s}^{-1}$ during T_{on} (170 ms). *b*, Schematic of the potential energy surface of the nuclear coordinates. Our analyses of the spectral trajectories indicate the existence of two distinctly different types of barrier heights. The small barriers are associated with fast thermal fluctuation (k_1), and the large (gross) barriers are associated with the photoinduced ($k_{2\text{pho}}$) and slow thermal ($k_{2\text{ther}}$) fluctuations.

rate ($k_{2\text{ther}}$), but is often dominated by the photoinduced rate ($k_{2\text{pho}} = k_2 - k_{2\text{ther}}$) for a broad range of excitation intensity. Although it is difficult to extrapolate the slower $k_{2\text{ther}}$ at zero excitation rate (Fig. 3*b*, *c*), $k_{2\text{ther}}$ can be determined by using the scheme shown in Fig. 4 inset and by evaluating the autocorrelation functions, $C(n)$, at different dark times, T_{off} . When neglecting the fast component k_1 ,

$$C(n) = C(0) \exp\{-nk_{2\text{ther}}(T_{\text{off}} + T_{\text{on}}) - nk_{2\text{pho}}T_{\text{on}}\} \\ = C(0) \exp(-n\gamma) \quad (2)$$

where $\gamma = k_{2\text{ther}}T_{\text{off}} + (k_{2\text{ther}} + k_{2\text{pho}})T_{\text{on}}$ is a single exponential rate constant. Therefore, a longer dark time results in a faster decay of $C(n)$, as is evident by comparing the decay of the curve in Fig. 4*b* to the slow component of the curve in Fig. 4*a*. In Fig. 5*a*, we plot γ as a function of T_{off} for several trajectories of a few molecules at a constant excitation rate during T_{on} . The slope of the fitted line gives $k_{2\text{ther}} = 0.02 \pm 0.01 \text{ s}^{-1}$, whereas the intercept results in $k_{2\text{pho}} = 0.02 \pm 0.01 \text{ s}^{-1}$.

The large k_1 and the small $k_{2\text{ther}}$ indicate that there are two distinctly different types of barrier in the potential-energy surface of the nuclear coordinates. As illustrated schematically in a one-dimensional cross-section of the ground-state potential energy surface (Fig. 5*b*), the local potential minima connected with the small barriers can be accessed through the fast thermal fluctuation (k_1), whereas the gross potential minima connected with the large barriers can only be accessed through the slow photoinduced fluctuation ($k_{2\text{pho}}$) and the much slower thermal fluctuation ($k_{2\text{ther}}$). Within each gross minimum, there is a spectral mean distribution (with variance of σ_1^2) associated with the different local minima. Independently, there is another spectral mean distribution (with variance of σ_2^2) associated with the different gross minima. The activation energies for k_1 and $k_{2\text{ther}}$ might be evaluated from the temperature dependence of the spectral trajectories.

Although a microscopic description of the nuclear coordinates

awaits further studies, our room-temperature experiments have provided new insights into the general features of the potential-energy surface and the dynamical properties of a single molecule in a particular environment. Similar structures of potential energy surfaces have been put forward for proteins¹⁸, and the kind of analysis described here may allow them to be explored. □

Received 22 May; accepted 18 November 1996.

1. Betzig, E. & Chichester, R. J. *Science* **262**, 1422–1425 (1993).
2. Nie, S., Chiu, D. T. & Zare, R. N. *Science* **266**, 1018–1021 (1994).
3. Macklin, J. J., Trautman, J. K., Harris, T. D. & Brus, L. E. *Science* **272**, 255–258 (1996).
4. Trautman, J. K., Macklin, J. J., Brus, L. E. & Betzig, E. *Nature* **369**, 40–42 (1994).
5. Xie, X. S., Bian, R. X. & Dunn, R. C. in *Focus of Multidimensional Microscopy* Vol. 1 (eds Chen, P. C., Hwang, P. P., Wu, J. L., Wang, G. & Kim, H.) (World Scientific, Teaneck, NJ, in the press).
6. Xie, X. S. & Dunn, R. C. *Science* **265**, 361–364 (1994).
7. Ambrose, W. P., Goodwin, P. M., Martin, J. C. & Keller, R. A. *Science* **265**, 364–367 (1994).
8. Bian, R. X., Dunn, R. C., Xie, X. S. & Leung, P. T. *Phys. Rev. Lett.* **75**, 4772–4775 (1995).
9. Schmidt, Th., Schutz, G. J., Baumgartner, W., Gruber, H. J. & Schindler, H. J. *Phys. Chem.* **99**, 17662–17668 (1995).
10. Bernard, J., Fleury, L., Talon, H. & Orrit, M. J. *Chem. Phys.* **98**, 850–859 (1993).
11. Basche, Th., Kummer, S. & Brauchle, C. *Nature* **373**, 132–134 (1995).
12. Ambrose, P. A. & Moerner, W. E. *Nature* **349**, 225–227 (1991).
13. Reilly, P. D. & Skinner, J. L. J. *Chem. Phys.* **102**, 1540–1552 (1995).
14. Jankowiak, R. & Small, G. J. *Science* **237**, 618–625 (1987).
15. Orrit, M. & Bernard, J. *Phys. Rev. Lett.* **65**, 2716–2719 (1990).
16. Moerner, W. E. et al. *J. Phys. Chem.* **98**, 7382–7389 (1994).
17. Basche, Th., Ambrose, W. P. & Moerner, W. E. *J. Opt. Soc. Am. B* **9**, 829–836 (1992).
18. Frauenfelder, H. & Wolynes, P. G. *Phys. Today* **47**, 58–64 (1994).

ACKNOWLEDGEMENTS. We thank R. Dunn, J. Trautman, P. Barbara, K. Eisenthal, C. Johnson, S. Colson and G. Holtom for discussions. Pacific Northwest National Laboratory is operated for the US Department of Energy (DOE) by Battelle. This work was supported by the Office of Basic Energy Sciences, Chemical Science Division, US DOE.

CORRESPONDENCE should be addressed to X.S.X. (e-mail: xs_xie@pnl.gov).

Silurian hydrothermal-vent community from the southern Urals, Russia

Crispin T. S. Little*, Richard J. Herrington*, Valeriy V. Maslennikov†, Noel J. Morris* & Viktor V. Zaykov†

* The Natural History Museum, Cromwell Road, London SW7 5BD, UK
† Institute of Mineralogy, Urals Branch Russian Academy of Sciences, Miass, Chelyabinsk district 456301, Russia

MODERN hydrothermal-vent communities are remarkable for being dependent on bacterial chemosynthetic primary production and for having a high percentage of endemic taxa (95% at the species level)^{1–3}. Based on phylogenetic analyses, it has been suggested that some of these taxa are Mesozoic or even Palaeozoic relicts, and that the vent environment has thus acted as a refuge against evolutionary pressures, such as mass extinctions, that affect other ecosystems^{1,2,4}. However, little is known about ancient vent communities because fossils have been reported from very few^{5–11} of a thousand or so documented vent deposits¹². Here we describe a macrofossil assemblage of monoplacophoran molluscs, inarticulate brachiopods, vestimentiferan tube-worms and other tubes, probably of polychaete origin, from the Silurian Yaman Kasy deposit¹². The assemblage represents the oldest, and most diverse, fossil hydrothermal-vent community known, and shares vestimentiferan and polychaete tube-worms with both modern vent communities^{1,2} and other ancient vent assemblages^{7–12}, but is unique in having brachiopods and monoplacophorans. Modern vent communities are not refuges for these Silurian shelly vent taxa, a finding that may have implications for the refuge hypothesis.

The Yaman Kasy volcanogenic massive sulphide deposit (Orenburg district, southern Urals, Russia) formed in a Silurian back-arc basin^{13–16}, and can be compared directly to modern sea-floor back-arc vent deposits¹⁷ on the basis of similarities in primary mineralogical textures and palaeo-fluid temperatures (R.J.H.,